



Nanoscale

**Silver telluride nanoparticles as biocompatible and enhanced contrast agents for x-ray imaging: an in vivo breast cancer screening study**

Journal:	<i>Nanoscale</i>
Manuscript ID	NR-ART-07-2020-005489.R2
Article Type:	Paper
Date Submitted by the Author:	22-Nov-2020
Complete List of Authors:	Nieves, Lenitza; University of Pennsylvania, Biochemistry and Molecular Biophysics Hsu, Jessica; University of Pennsylvania, Bioengineering Lau, Kristen; University of Pennsylvania, Bioengineering Maidment, Andrew; University of Pennsylvania, Radiology Cormode, David; University of Pennsylvania, Radiology

SCHOLARONE™  
Manuscripts

# Silver telluride nanoparticles as biocompatible and enhanced contrast agents for x-ray imaging: an *in vivo* breast cancer screening study

*Lenitza M. Nieves, Jessica C. Hsu, Kristen C. Lau, Andrew D. A. Maidment,*

*and David P. Cormode\**

Biochemistry and Molecular Biophysics Department, University of Pennsylvania,

Philadelphia, USA

Bioengineering Department, University of Pennsylvania, Philadelphia, USA

Radiology Department, University of Pennsylvania, Philadelphia, USA

Silver Telluride, Nanoparticles, Silver chalcogenides, Computed Tomography, Dual-energy Mammography, Contrast Agents

**Abstract** Silver sulfide nanoparticles ( $\text{Ag}_2\text{S}$  NPs) have gained considerable interest in the biomedical field due to their photothermal ablation enhancement, near-infrared fluorescence properties, low toxicity levels, and multi-imaging capabilities. Silver telluride nanoparticles ( $\text{Ag}_2\text{Te}$  NPs) have similar properties to  $\text{Ag}_2\text{S}$  NPs, should also be stable due to an extremely low solubility product and should generate greater x-ray contrast since tellurium is significantly more attenuating than sulfur at diagnostic x-ray energies. Despite these attractive properties,  $\text{Ag}_2\text{Te}$  NPs have only been studied *in vivo* once and at a low dose ( $2 \text{ mg Ag kg}^{-1}$ ). Herein, for the first time,  $\text{Ag}_2\text{Te}$  NPs' properties and their application in the biomedical field were studied *in vivo* in the setting requiring the highest nanoparticle doses of all biomedical applications, *i.e.* x-ray imaging.  $\text{Ag}_2\text{Te}$  NPs were shown to be stable, biocompatible (no acute toxicity observed in the cell lines studied or *in vivo*), and generated higher contrast, compared to controls, in the two x-ray imaging techniques studied: computed tomography (CT) and dual-energy

mammography (DEM). In summary, this is the first study where Ag<sub>2</sub>Te NPs were explored *in vivo* at a high dose. Our findings suggest that Ag<sub>2</sub>Te NPs provide strong x-ray contrast while exhibiting excellent biocompatibility. These results highlight the potential use of Ag<sub>2</sub>Te NPs in the biomedical field and as x-ray contrast agents for breast cancer screening.

Nanomaterials are known for their unique physical and chemical properties including their exceptional optical characteristics, ability to be engineered to obtain desired properties through the modification of their surface, size, and composition, as well as their tunable pharmacokinetics. These unique characteristics have led to the exploration of nanomaterials in biomedical applications,<sup>1</sup> such as fluorescence imaging and sensing probes,<sup>2</sup> drug delivery vehicles,<sup>3</sup> theranostic agents,<sup>4</sup> and contrast agents for several medical imaging techniques,<sup>5-8</sup> and have been key to innovation and progression in the field. Recently, several groups, including ours, have studied silver chalcogenides such as silver sulfide ( $\text{Ag}_2\text{S}$  NP) and silver selenide nanoparticles ( $\text{Ag}_2\text{Se}$  NP) in the biomedical field due to their photothermal ablation enhancement, near-infrared fluorescence properties, low toxicity levels, and x-ray contrast generation.<sup>9-14</sup>

In addition to  $\text{Ag}_2\text{S}$  and  $\text{Ag}_2\text{Se}$ , the silver chalcogenide group also includes silver telluride ( $\text{Ag}_2\text{Te}$ ).  $\text{Ag}_2\text{Te}$  has an extremely low solubility product ( $K_{\text{sp}} = 2 \times 10^{-72}$ ),<sup>15</sup> much lower than those of  $\text{Ag}_2\text{S}$  and  $\text{Ag}_2\text{Se}$  ( $6 \times 10^{-50}$  and  $3 \times 10^{-65}$ , respectively), and could consequently also have excellent stability and biocompatibility<sup>16, 17</sup>. Moreover, tellurium generates similar x-ray attenuation to silver, whereas the attenuation of sulfur and

selenium is negligible at diagnostic energies, therefore the x-ray attenuation of  $\text{Ag}_2\text{Te}$  should be substantially higher than for  $\text{Ag}_2\text{S}$  and  $\text{Ag}_2\text{Se}$ .<sup>18</sup> However, despite their outstanding properties,  $\text{Ag}_2\text{Te}$  NPs have been rarely explored in biomedical applications.  $\text{Ag}_2\text{Te}$  NPs have been explored as surface-enhanced Raman sensors and their NIR-II imaging properties have been characterized.<sup>19, 20</sup> However, only one other study to date has explored the biomedical application of  $\text{Ag}_2\text{Te}$  NPs *in vivo*, and at a low  $\text{Ag}_2\text{Te}$  NP dose.<sup>21</sup>

In this study, we propose taking advantage of the attractive properties of  $\text{Ag}_2\text{Te}$  NP to further explore their application in the biomedical field. We, therefore, tested  $\text{Ag}_2\text{Te}$  NPs in the setting that requires the highest nanoparticle doses of all biomedical applications, *i.e.* x-ray imaging.<sup>22</sup> We hypothesized that  $\text{Ag}_2\text{Te}$  NPs can be excellent contrast agents for two main x-ray imaging modalities: computed tomography (CT) and dual-energy mammography (DEM). CT is the most widely used x-ray imaging technique for whole-body imaging, while DEM is a newly developed multi-energy mammography technology approved for breast cancer screening. Currently, both x-ray imaging modalities rely on iodine-based contrast agents, which have been linked with contrast-induced

nephropathy and allergic reactions.<sup>23</sup> We hypothesize that Ag<sub>2</sub>Te NPs will meet the needs of both x-ray imaging techniques, with higher contrast than Ag<sub>2</sub>S NPs due to the presence of tellurium, while exhibiting excellent biocompatibility. In addition to silver chalcogenides, other metal nanoparticles including gold (Au) and Bismuth (Bi) have been widely used in x-ray imaging owing their high k-edge and x-ray attenuation coefficient in addition to their good biocompatibility.<sup>24,5</sup> However, the k-edges of these materials are not suitable for DEM x-ray imaging for breast cancer screening, where Ag<sub>2</sub>Te exhibits high contrast.<sup>18</sup> In addition, silver chalcogenides are of significantly lower cost than Au nanoparticles (i.e. \$63/g Au vs \$0.89/g Ag), and thus could be more accessible to patients.

In this study, Ag<sub>2</sub>Te NPs were characterized using transmission electron microscopy (TEM), dynamic light scattering (DLS), UV-vis spectroscopy, energy dispersive x-ray spectroscopy (EDX), x-ray powder diffraction (XRD) as well as inductively coupled plasma optical emission spectroscopy (ICP-OES). We tested the biocompatibility of the nanoparticles through a series of experiments both, *in vitro*, through cell viability in different cell lines, and *in vivo*, through histology analysis. Moreover, their ability to be

used as x-ray contrast agents was explored in an *in vitro* setting using different x-ray imaging modality phantoms, as well as *in vivo* through CT imaging of breast cancer tumor-bearing mice. Furthermore, the biodistribution of these nanoparticles in mice was also analyzed.

### ***Materials and Methods***

#### **Materials**

Silver nitrate ( $\text{AgNO}_3$ ), sodium borohydride ( $\text{NaBH}_4$ ), and sodium citrate ( $\text{Na}_3\text{C}_6\text{H}_5\text{O}_7$ ) were purchased from Sigma-Aldrich (St. Louis, MO). Sodium tellurite ( $\text{Na}_2\text{TeO}_3$ ) was purchased from Alfa Aesar (Haverhill, MA). Hydrazine ( $\text{N}_2\text{H}_4$ ) 80% and nitric acid ( $\text{HNO}_3$ ) were purchased from Acros Organics (Thermo Fisher Scientific, NJ) and Fisher Chemical (Thermo Fisher, Waltham, MA), respectively. Monofunctional PEG thiol (mPEG-SH) 5K was purchased from Creative PEGworks (Chapel Hill, NC). Milli-Q deionized water (18.2  $\text{M}\Omega\cdot\text{cm}$ ) was used throughout the experiments.

#### **Nanoparticle syntheses**

##### **Silver telluride nanoparticles**

The synthesis protocol of silver telluride nanoparticles ( $\text{Ag}_2\text{Te}$  NPs) was adapted from a previous report.<sup>20</sup> In brief, a 9 mL aqueous solution containing 5 mM of sodium tellurite, 10 mM of silver nitrate, and 30 mM of mPEG-SH 5K was prepared. 1 mL of hydrazine was quickly added to the previous solution. The mixture was then heated to 90 °C for 30 minutes under constant magnetic stirring. After the reaction was completed, the product was washed thrice, with DI water, by centrifugation using 10 kDa ultrafiltration molecular weight cut-off tubes (MWCO) at 4000 rpm. Following the third wash, the nanoparticles were dispersed in DPBS and then washed by centrifugation at the above-mentioned speed and using the same size MWCO tubes. The nanoparticles were then concentrated to a final volume of 1 mL and filtered through a 0.22  $\mu\text{m}$  filter. The filtered nanoparticles were then stored at 4 °C for further use.

### **Silver nanoparticles**

Silver nanoparticles (Ag NPs) were prepared as described in our previous work.<sup>25</sup> In brief, 1.25 mL of 0.1 M sodium citrate were added to 500 mL of DI water, followed by the addition of 1.25 mL of 0.1 M silver nitrate and 5 mL of 0.1 M sodium borohydride. Next, 5 mL of 12.5 mg/mL mPEG-SH-5K were added to the reaction, which was left to

stir overnight. The resulting particles were purified thrice with DI water and concentrated by centrifugation using 10 kDa MWCO tubes at 4000 rpm. Following the third wash, the nanoparticles were dispersed in DPBS and then washed by centrifugation at the above-mentioned speed and using the same size MWCO tubes. The nanoparticles were then concentrated to a final volume of 1 mL and filtered through a 0.22  $\mu\text{m}$  filter. The filtered nanoparticles were then stored at 4 °C for further use.

### **Silver sulfide nanoparticles**

Silver sulfide nanoparticles ( $\text{Ag}_2\text{S}$  NPs) were prepared by mixing 0.375 mmoles of  $\text{AgNO}_3$  and 0.012 mmoles of mPEG-SH 5K in 75 mL of DI water, followed by the rapid addition of 0.38 mmoles of  $\text{Na}_2\text{S}$  in 25 mL of DI water at ambient conditions. The reaction was allowed to stir overnight at room temperature. The resulting particles were purified three times with DI water and concentrated by centrifugation using 10 kDa MWCO tubes at 4000 rpm. Following the third wash, the nanoparticles were dispersed in DPBS and then washed by centrifugation at the above-mentioned speed and using the same size MWCO tubes. The nanoparticles were then concentrated to a final

volume of 1 mL and filtered through a 0.22  $\mu\text{m}$  filter. The filtered nanoparticles were then stored at 4  $^{\circ}\text{C}$  for further use.

## **Nanoparticle characterization**

### **Dynamic light scattering and zeta potential**

The hydrodynamic diameter and zeta potential of the nanoparticles were measured using a Zetasizer (Nano-ZS 90, Malvern instrument, Malvern, UK). The number mean was reported for the hydrodynamic diameter. All measurements were performed at 25  $^{\circ}\text{C}$ .

### **Transmission electron microscopy**

Nanoparticle core size was measured as described previously.<sup>9, 26</sup> JEOL 1010 and Tecnai T12 electron microscopes were used with an acceleration voltage of 80 and 100 kV, respectively. 10  $\mu\text{L}$  of the sample were placed onto Formvar carbon-coated copper grids with 200 mesh (Electron Microscopy Sciences, Hatfield, PA) and allowed to dry before imaging. ImageJ (National Institutes of Health, Bethesda, MD) was used to measure the core diameter of individual nanoparticles.

### **UV/visible absorption spectroscopy**

UV/visible spectra of silver telluride nanoparticles were recorded using a Genesys 150 UV/visible spectrophotometer (Thermo Scientific, USA). In brief, 5  $\mu\text{l}$  of the nanoparticle stock were diluted with 995  $\mu\text{l}$  of DI water.

### **Silver telluride nanoparticle stability study**

Silver telluride nanoparticles solutions with a concentration of 0.5 mg/mL were prepared in water, PBS and PBS + 10% FBS, in triplicate. UV/visible absorption spectra were obtained for each of the solutions in triplicate using the UV/visible spectrophotometer described above. The absorbance spectrum was normalized to a maximum absorbance of 1. The hydrodynamic diameter of the solutions was measured using the Zetasizer described above. The number mean was reported for the hydrodynamic diameter. Solutions were maintained at 25 °C. Both UV/visible spectra and hydrodynamic size were measured at different time points; 0, 1, 3,7, and 14 days post-dilution.

### **Inductively coupled plasma optical emission spectroscopy (ICP-OES)**

ICP-OES (Spectro Genesis ICP) was used to determine the silver and tellurium concentration in the nanoparticle formulation as previously described.<sup>9, 26</sup> In brief, 10  $\mu\text{L}$

of Ag<sub>2</sub>Te NP stock solution were placed in 15 mL falcon tubes. The nanoparticles were dissolved in 10% nitric acid. The final silver and tellurium concentrations in the stock solution were obtained by multiplying the concentrations obtained by the ICP-OES by their dilution factor.

### **Energy dispersive X-ray spectroscopy**

Similar to the transmission electron microscopy methodology, samples were dried onto Formvar carbon-coated copper grids with 200 mesh. The samples were then imaged using a FEI Quanta 600 field emission gun scanning electron microscope equipped with EDX detectors. The equipment was operated at 15 kV.

### **X-ray powder diffraction**

The diffraction patterns of dried samples were recorded using a Rigaku GiegerFlex D/Max-B X-ray diffractometer. The parameters used while operating the diffractometer were the following: 45 kV, 30 mA, monochromatized Cu K $\alpha$  radiation wavelength of 1.5406 Å, scan range of 20-60° and 2° per minute scan rate.

## **Cell Assays**

### **Cell Culture**

Hep G2 (human hepatocellular liver carcinoma), J774A.1 (murine macrophage), and MDA-MB-231 (human breast cancer) cells were purchased from ATCC (Manassas, VA, USA). Cells were cultured according to the supplier's instructions at 37 °C and 5% CO<sub>2</sub>.

### *In vitro* cytotoxicity

Cell viability studies were performed as described elsewhere.<sup>9, 26</sup> In brief, 80,000 cells were seeded in 35 mm dishes with 20 mm bottom well. These cells were incubated for 24 hours in the appropriate cell culture media. After the 24 hours, the cell culture media was removed, cells washed with DPBS, and a solution of Ag<sub>2</sub>Te or Ag nanoparticles diluted in cell media at different concentrations was added. The concentrations used in this experiment were 0.1, 0.5, and 1 mg Ag/mL. Cells were incubated for 4 hours with the appropriate nanoparticle type and concentrations. Cell viability was determined by LIVE/DEAD assay (Invitrogen Life Technologies, Grand Island, NY). Following the 4-hour incubation period, cells were washed with sterile DPBS, and 400 µL of a solution containing the live cell dye calcein-AM, dead cell dye ethidium-1 homodimer, and nuclei dye Hoechst 33342 in DPBS was added. Cells were incubated with this dye solution for 20 minutes. The cells were then imaged using a Nikon Eclipse Ti-U fluorescence

microscope with DAPI (ex: 359, em: 461 nm), FITC (ex: 495, em: 519 nm), and Texas Red (ex: 595, em: 613 nm) filters to image nuclei, live cells, and dead cells, respectively. Four phase images, as well as four images per filter, were taken for each plate. The number of live and dead cells was measured using an in-house developed MATLAB (MathWorks, Natick, MA) code. The viability percentage was determined by the ratio of live cells to dead cells. The relative cell viability (% control) is presented as mean  $\pm$  standard deviations for each concentration and cell line.

### **Phantom imaging**

#### **Computed tomography**

For CT phantom studies, solutions composed of Ag<sub>2</sub>Te NPs, silver (AgNO<sub>3</sub>), tellurium (Na<sub>2</sub>TeO<sub>3</sub>), and iodine (iopamidol) at concentrations ranging from 0 to 10 mg of the element of interest/mL were prepared and placed in small vials. PBS was used as a negative control. Each solution was prepared in triplicate. These vials were then secured in a plastic rack. The rack was then submerged in a plastic container holding 21 cm of water to simulate the human abdominal cavity. The samples were imaged using a Siemens SOMATOM Force clinical CT scanner. The images were obtained at

tube voltages ranging from 80 to 140 kV in 20 kV increments with a tube current of 360 mA. The field of view used measured 37 x 37 cm while the slice thickness was 0.5 mm and the matrix size was 512 x 512. The obtained images were then analyzed using OsirixMD. The attenuation rates were calculated from the average of three slices per sample.

### Dual-energy mammography

Dual-energy mammography images in a custom-designed wedge phantom (Supplemental Figure 20) were acquired for the study. The phantom consists of a 4 cm-thick continuous gradient section composed of tissue-equivalent materials ranging in composition from 100% glandular tissue to 100% adipose tissue, as previously described.<sup>27</sup> Solutions of Ag<sub>2</sub>Te NPs, iodine (in the form of iopamidol), silver salt (AgNO<sub>3</sub>), and tellurium salt (Na<sub>2</sub>TeO<sub>3</sub>) were loaded into polyethylene tubes at a concentration of 10 mg of the element of interest/mL; PBS was used as a control. The tubes were inserted into the phantom in the direction of varying tissue composition.

Images of the phantom were then acquired using a prototype DE Hologic Selenia Dimensions mammography system. The imaging system consists of an x-ray source

with a tungsten target and an energy-integrating selenium detector. Low-energy (LE) images of the phantom were acquired at 29 kV using a silver filter at 100 mAs; High-energy (HE) images of the phantom were acquired at 38 kV using a copper filter at 90 mAs. Each tube was imaged in triplicate.

DE image subtraction was performed to eliminate variations in the tissue background so that we could differentiate the attenuation of the contrast agent signal from the soft tissue signal. DE images of the phantoms were obtained by a weighted logarithmic subtraction of the HE and LE image pairs. The DE subtraction process and contrast-to-noise (CNR) calculations are described in further detail in our previous works.<sup>26, 27</sup>

### *In vivo* experiments

#### **Animal tumor model**

All animal procedures were performed following the Public Health Service (PHS) Policy on Humane Care and Use of Laboratory Animals (Public Law 99-158) in accordance with the University of Pennsylvania Guidelines for Care and Use of Laboratory Animals and approved by the Institutional Animal Care and Use Committee (IACUC) of the University of Pennsylvania under protocol number 805593.

For *in vivo* assessments, an orthotopic tumor model was developed. For this,  $2.5 \times 10^6$  MDA-MB-231 cells were implanted in the fourth mammary pads of 12 nude female mice. Tumor growth and mouse health were monitored weekly. Tumor volume was measured with calipers and calculated using the following equation: Tumor volume =  $\frac{1}{2}$  (length  $\times$  width<sup>2</sup>). Mice with tumors with an average volume of 100 mm<sup>3</sup>, were injected via the tail vein with Ag<sub>2</sub>Te NPs or Ag<sub>2</sub>S NPs (as a control) at a dose of 250 mg/kg (190  $\mu$ L injection volume). This dose was chosen since it is comparable to the iopamidol dose used for patients.<sup>28</sup> Isoflurane was used to anesthetize mice during all experiments.

### Computed tomography

*In vivo* CT imaging was performed using a Molecubes X-Cube micro-CT scanner. Images were acquired using the following parameters: 50 kVp, 100 $\mu$ A, 85ms exposure, and 480 projections. Images were reconstructed through a software provided by the manufacturer and using 100  $\mu$ m isotropic voxel reconstruction with a noise regularization factor of 3. Mice were scanned before injection, 2 hours post-injection and 24 hours post-injection. The obtained images were analyzed using OsirixMD. For the

analysis, ROIs were drawn in the organs of interest and the attenuation values (HU) were recorded. The data is presented as the change in attenuation from pre-injection scans as mean  $\pm$  standard deviation.

### **Biodistribution**

The biodistribution experiment was performed in 10 female wild-type mice. 24 hours post-injection, mice were euthanized with CO<sub>2</sub> gas for 10 minutes according to the IACUC approved protocol. Mice were then dissected and tissue from the heart, liver, kidney, spleen, and lungs were collected and their weights were recorded. These tissues were then minced and subjected to acid digestion with 2 mL of nitric acid overnight at 75 °C. The samples were then diluted to a final volume of 10 mL with DI water. The silver and tellurium concentrations were measured for the tissue of mice injected with Ag<sub>2</sub>Te NPs while the silver concentration was measured for tissue from mice injected with Ag<sub>2</sub>S NPs. The concentration of metals was determined through ICP-OES. An average of 5 mice per group were analyzed. Biodistribution data is presented as mean  $\pm$  standard error of mean (SEM).

### **Histology**

Following mice euthanasia, tissues from the major organs (heart, liver, spleen, lung, and kidney) of 2 mice per group, were collected and sliced into 5-6 mm in thickness while placed in chilled PBS. Tissues were immediately fixed in a 10% formalin solution at 4 °C overnight. The samples were then dehydrated, embedded, sectioned, and stained with hematoxylin and eosin (H&E) by the Children's Hospital of Philadelphia Pathology Core.

### **Statistical Analysis**

All the experiments were performed independently at least three times. In all figures, data points represent the mean, while the error bars represent standard deviations from the mean or the standard error of mean, as specified. Tukey's multiple comparisons test was used when comparing the stability of Ag<sub>2</sub>Te NPs via size measurements, the CNR of different solutions in the DEM phantom, and the attenuation rate of the different solutions under CT. Unpaired t-tests were used to compare between cell viability data from Ag and Ag<sub>2</sub>Te NPs and when comparing among Ag<sub>2</sub>Te and Ag<sub>2</sub>S *in vivo* CT attenuation. P values  $\leq 0.05$  were considered statistically significant. Statistical analysis was carried out using GraphPad Prism 8 software (San Diego, California USA).

## *Results and Discussion*

### **Synthesis and characterization of Ag<sub>2</sub>Te NPs**

Ag<sub>2</sub>Te nanoparticles were synthesized as depicted in **Figure 1A**, where silver nitrate and sodium tellurite were used as silver and tellurium precursors, respectively, and reduced by hydrazine dihydrate. The Ag<sub>2</sub>Te NPs were coated with 5K polyethylene glycol thiol (PEG-SH) for improved stability, biocompatibility, and blood circulation half-life. An electron micrograph from the resulting nanoparticles is shown in **Figure 1B** and Supplemental Figure 3A. The nanoparticle core size, measured from the electron micrographs, was found to be  $8 \pm 2$  nm in diameter, while the hydrodynamic diameter was determined to be  $17 \pm 5$  nm *via* DLS measurements. This difference in diameter between the core and the hydrodynamic diameter is expected due to the PEG coating and is in agreement with previous reports of PEG-SH 5K coated nanoparticles. For example, Silvestri, *et al*/has reported a difference of 11 nm while Chen *et al*/reported an increase of 6 nm.<sup>25, 29</sup> The Z-potential of the nanoparticles was also measured and resulted in  $-14.9 \pm 0.8$  mV, which is consistent with other reports of slightly negative or

neutral PEGylated nanoparticles.<sup>26, 30-32</sup> These results are summarized in **Figure 1D**. 11-mercaptopundecanoic acid (11-MUA) coated Ag<sub>2</sub>Te NPs were synthesized as a control nanoparticle with an anionic surface and their Z-potential was found to be  $-48 \pm 10$  mV (Supplemental Figure 1). To further characterize the Ag<sub>2</sub>Te NPs, their UV-vis spectrum was recorded and is shown in **Figure 1C**. This broad spectrum reveals a profile characteristic of Ag<sub>2</sub>Te nanoparticles where no prominent peak is observed,<sup>16, 33</sup> as compared to pure silver nanoparticles (Ag NPs) that have a peak at a wavelength of near 400 nm (Supplemental Figure 2). A high-resolution TEM micrograph of the Ag<sub>2</sub>Te NPs is presented in Supplemental Figure 4A. We further characterized the optical properties of our Ag<sub>2</sub>Te NP formulation, specifically their fluorescence properties. Although other silver chalcogenide nanoparticles have been previously reported to yield fluorescence in the NIR regions, we did not observe fluorescence from this formulation.<sup>34, 35</sup> We hypothesize that this is due to the synthesis being carried out in aqueous conditions, which have been previously reported to result in low fluorescent yields.<sup>34, 36</sup>

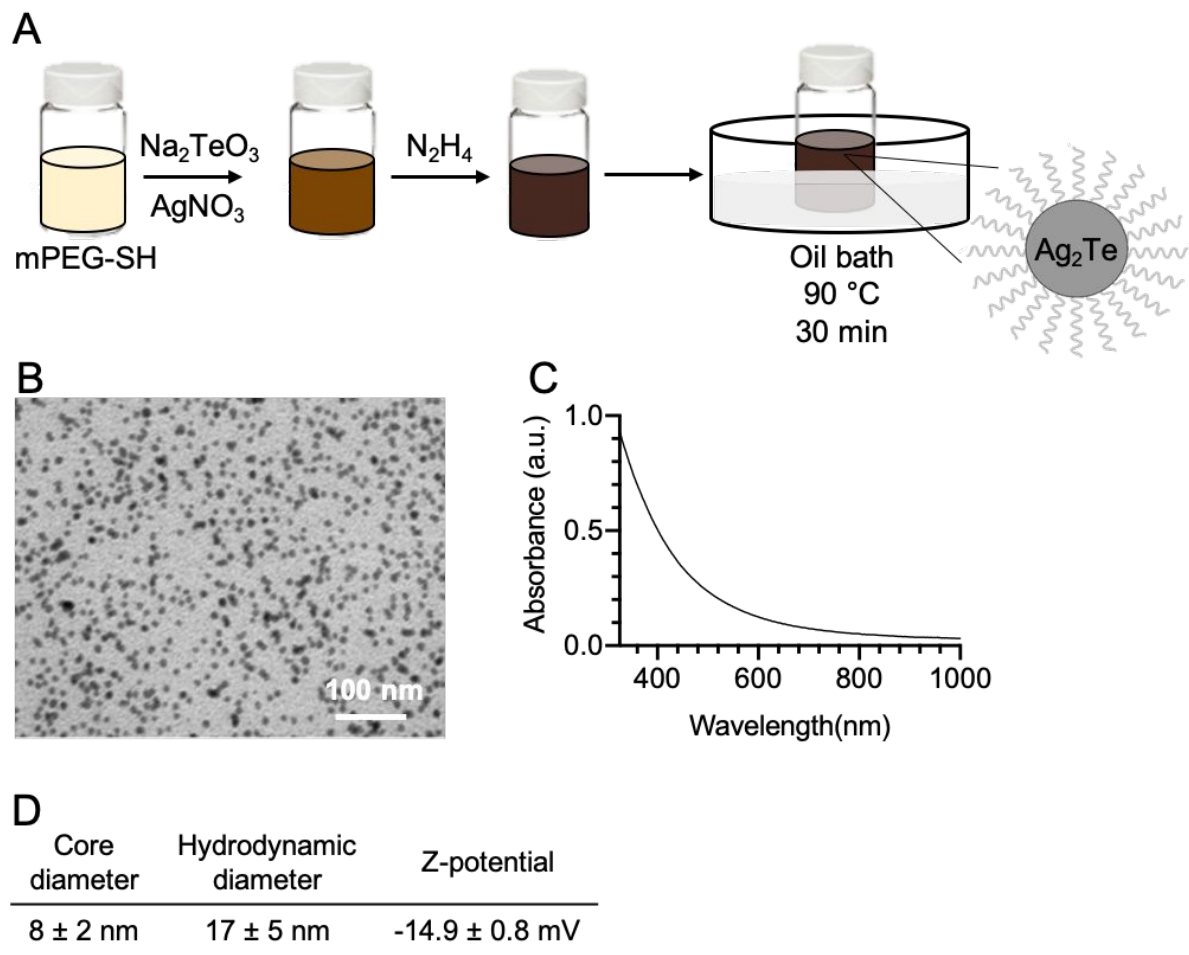


**Figure 1:**  $\text{Ag}_2\text{Te}$  nanoparticle synthesis and characterization. A) Schematic depiction of  $\text{Ag}_2\text{Te}$  NP synthesis. B) Transmission electron micrograph of  $\text{Ag}_2\text{Te}$  NPs. C) UV-visible absorbance spectrum of  $\text{Ag}_2\text{Te}$  NPs. D) Table summarizing  $\text{Ag}_2\text{Te}$  NP core diameter, hydrodynamic diameter, and z-potential values.

To investigate the composition of the  $\text{Ag}_2\text{Te}$  NPs further, we performed energy dispersive x-ray spectroscopy (EDX). The obtained spectrum is presented in **Figure 2A**. In this spectrum, we can observe peaks at an x-ray energy of 2.98 keV, 3.77 keV, and 2.3 keV corresponding to silver, tellurium, and sulfur respectively. Furthermore, the silver and tellurium peaks show a 2:1 ratio as expected. ICP-OES measurements also confirmed the 2:1 ratio of silver to tellurium (data not shown). To further characterize the  $\text{Ag}_2\text{Te}$  NPs, an XRD spectrum was obtained and shown in **Figure 2B**. Although broad peaks are observed due to the small size of the nanoparticle core, the strong peaks at 27, 36, and 41  $2\theta$  degrees closely matches that of previously reported  $\text{Ag}_2\text{Te}$  XRD patterns<sup>37, 38</sup>, while the peak at 24  $2\theta$  degrees matches that of PEG.<sup>39, 40</sup> Moreover, the  $\text{Ag}_2\text{Te}$  nanoparticles were further characterized using XPS. The resulting spectra are presented in Supplemental Figure 5. This data further confirms the oxidation of Ag and the presence of Te in the samples. The peaks at 366.4 eV and 372.4 eV correspond to Ag 3d 5/2 and Ag 3d 3/2, respectively while those at 570.4 eV and 581.4 eV correspond to Te 3d 5/2 and Te 3d 3/2, respectively.

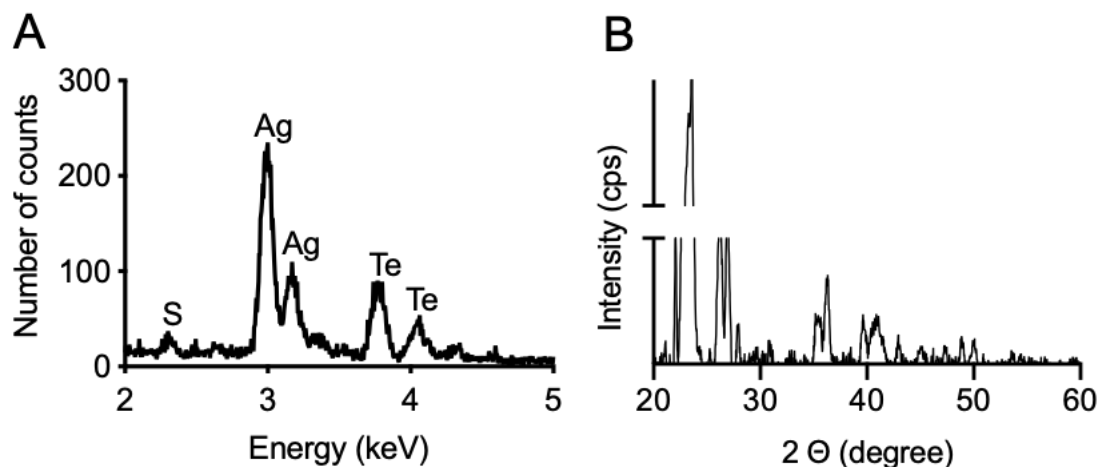


**Figure 2:** A) Energy dispersive x-ray spectrum of  $\text{Ag}_2\text{Te}$  nanoparticles. B) XRD spectrum of  $\text{Ag}_2\text{Te}$  nanoparticles.

An important characterization assay to aid in predicting nanoparticle *in vivo* performance is the determination of the stability of the nanoparticles in biologically relevant media. To test this, the nanoparticles were incubated in DI water, PBS, and PBS + 10% FBS to assess their stability in the absence and presence of ions as well as in the presence of both ions and serum proteins. These different solutions were analyzed with UV-vis (**Figure 3A-C**) and DLS (**Figure 3D-F**) since these two techniques are sensitive to particle size and concentration. The solutions were incubated at room

temperature for fourteen days. As shown in **Figure 3**, there was no significant change in the UV-vis spectra from the initial incubation time over this time period. Similarly, no significant difference was observed in the hydrodynamic diameter in any of the media tested. These results show the high stability of these nanoparticles in the different conditions and more importantly, in PBS + 10% FBS, which more closely represents the *in vivo* conditions. Complementary, the stability of Ag<sub>2</sub>Te NPs was monitored by TEM and XRD. Results are presented in Supplemental Figure 6 and 7. The constant size of the NPs observed in TEM samples and the consistent peaks near 27, 36, and 41 2  $\theta$  degrees observed with XRD throughout 14 days, further confirms the high stability of the NPs. The peaks at 32, 45, and 56 2 $\theta$  degrees correspond to NaCl found in PBS, while the peak at 24 2 $\theta$  degrees correspond to mPEG-SH 5K, as previously mentioned. Supplemental Figure 8 shows the stability of Ag<sub>2</sub>Te NPs coated with 11-MUA as a control. The decrease in absorbance for 11-MUA coated Ag<sub>2</sub>Te NPS indicates aggregation and therefore inferior stability. To further investigate the degradation of Ag<sub>2</sub>Te nanoparticles, we incubated them in water and simulated lysosomal fluid and measured the release of Ag<sup>+</sup> ions. Results are presented in Supplemental Figure 9. Our

results are in agreement with previous reports where  $\text{Ag}_2\text{S}$  released less  $\text{Ag}^+$  ions in both conditions compared to  $\text{Ag}$  nanoparticles.<sup>10</sup> The stability data of PEG-SH 5K coated  $\text{Ag}_2\text{Te}$  NPs, together with other characterizations including the close to neutral Z-potential (Supplemental Figure 1), XRD peak at  $24\ 2\theta$  degrees, EDX sulfur peak, and FT-IR (Supplemental Figure 10) suggest the successful PEGylation of the  $\text{Ag}_2\text{Te}$  nanoparticles.<sup>31, 39, 40.</sup>

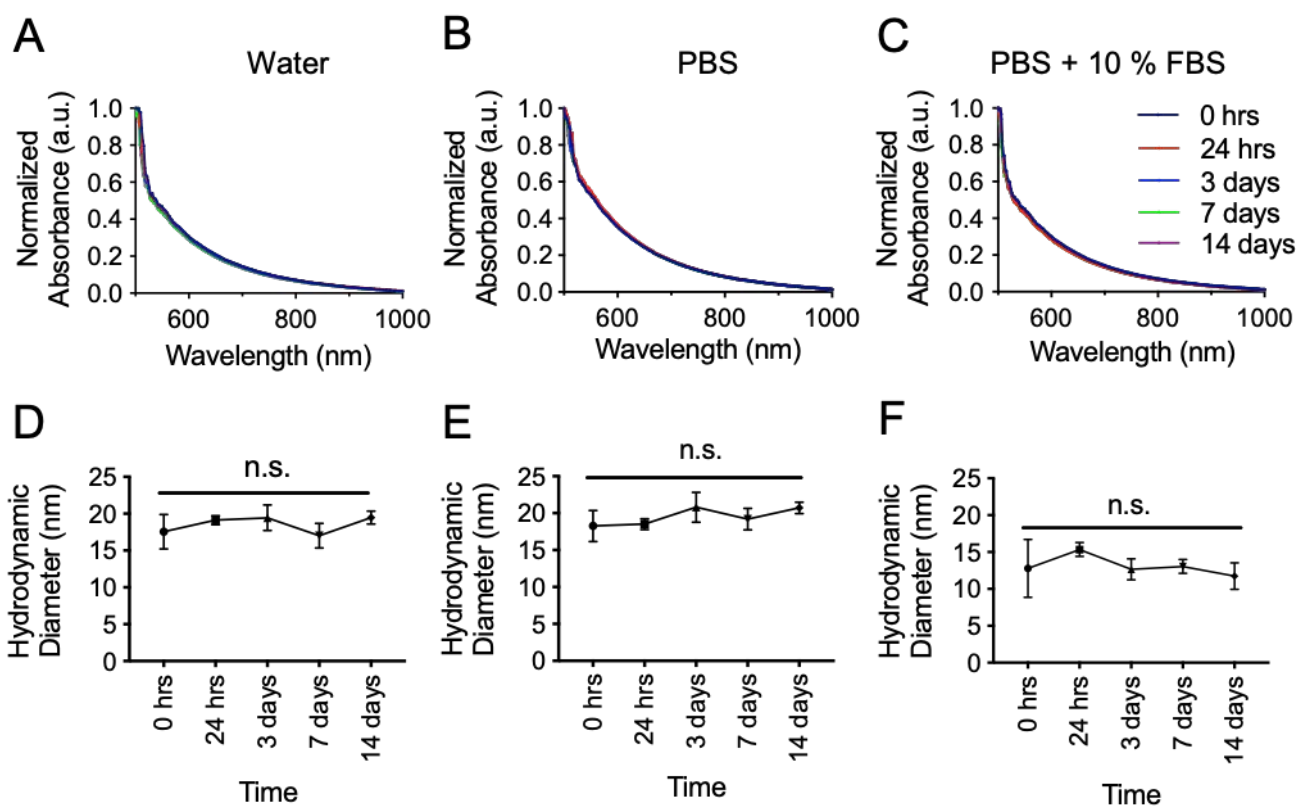


**Figure 3:** UV-Vis spectra of Ag<sub>2</sub>Te nanoparticles incubated in A) DI water, B) PBS and C) PBS + 10% FBS for 14 days. The dark blue curve shows data from day 0, red from 24 hrs, blue from 3 days, green from 7 days, and purple from 14 days post-incubation in the different media. The hydrodynamic diameter of Ag<sub>2</sub>Te nanoparticles in D) DI water, E) PBS, and F) PBS + 10% FBS. Data is presented as the mean, while the error bars represent standard deviations.

**Ag<sub>2</sub>Te nanoparticles show no acute toxicity when incubated with different cell lines.**

Prior to *in vivo* testing, an *in vitro* assay was conducted where nanoparticles were incubated with different cell types. For this, we studied the effect of the nanoparticles in the viability of specific cell types where they are predicted to accumulate. Due to their size, these nanoparticles are predicted to accumulate in the reticuloendothelial system (RES) organs such as the liver and spleen.<sup>41-43</sup> These nanoparticles should also accumulate in the tumor due to the enhanced permeability and retention (EPR) effect. For this reason, we studied the viability of liver, macrophage, and breast cancer tumor

cell lines after incubation with the nanoparticles. Furthermore, the effect of Ag<sub>2</sub>Te NPs in these different cell lines was compared to that of pure silver nanoparticles (Ag NPs) which have been shown previously to be toxic to cells due to their release of pure silver ions.<sup>44</sup> As an additional control, the viability of cells after incubation with Ag<sub>2</sub>S NPs was also measured. For this, Ag NPs and Ag<sub>2</sub>S of the same size and coating were synthesized, and their characterization is presented in Supplemental Figures 2, 3, 4, 11, 12 and 13. In this experiment, the different cell types were incubated with Ag<sub>2</sub>Te NPs and Ag or Ag<sub>2</sub>S NPs, as controls, for 4 hours (**Figure 4**). The cytotoxic effect of the Ag NPs in all three cell lines at concentrations higher than 0.1 mg Ag/mL are readily apparent. In contrast, no acute toxicity was observed with Ag<sub>2</sub>Te NPs (no significant difference from control) with all three cell lines up to the highest concentration tested (*i.e.* 1 mg Ag/mL). Similar results were obtained from Ag<sub>2</sub>S NPs, in agreement with previous reports.<sup>9</sup> To further look into the biocompatibility of these nanoparticles, we have included the data on the generation of ROS and DNA damage in macrophages. Results are presented in Supplemental Figure 14 and 15. Increase ROS generation can be observed for Ag nanoparticles compared to Ag<sub>2</sub>Te and Ag<sub>2</sub>S at 0.25 mg/mL whereas

at higher concentrations the decrease in ROS is supported by our cell viability data where these cells are no longer viable and thus we detect lower levels of ROS. These data support our cell viability data where no acute toxicity was observed after incubation with  $\text{Ag}_2\text{Te}$  nanoparticles as compared to  $\text{Ag}$  nanoparticles and the similarity in biocompatibility with  $\text{Ag}_2\text{S}$  nanoparticles.

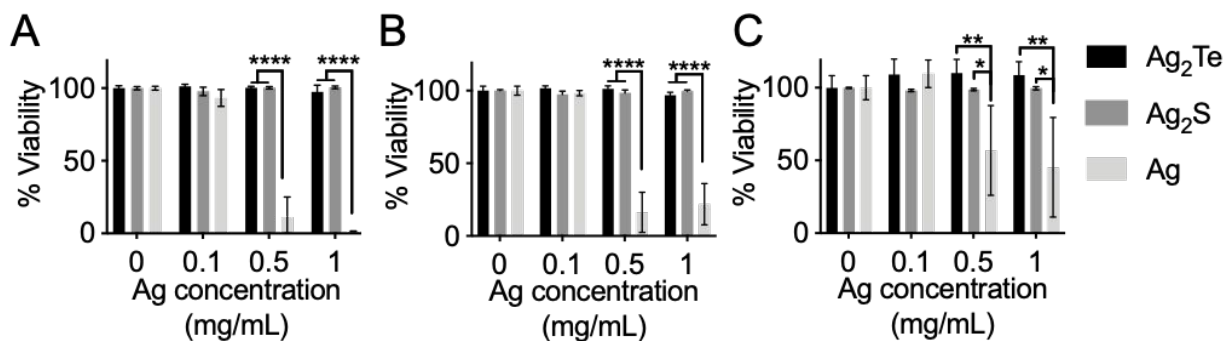


**Figure 4:** Viability of A) HepG2, B) MDA-MB-231 and C) J774A.1 cells after incubation with  $\text{Ag}_2\text{Te}$  (black bars),  $\text{Ag}_2\text{S}$  (dark gray) or  $\text{Ag}$  NPs (silver bars) for 4 hours. Error bars represent standard deviations. \*P-value < 0.05. \*\* P-value ≤ 0.01 \*\*\*\* P-value < 0.0001.

$\text{Ag}_2\text{Te}$  NPs generate higher contrast in CT and DEM phantoms compared to silver and iopamidol

The ability of Ag NPs to be used as x-ray contrast agents has been previously investigated.<sup>25, 42</sup> It has been shown that Ag NPs can produce slightly less contrast in CT and 40% higher contrast in DEM compared to iodinated molecules currently used in the clinics.<sup>25, 45</sup> Similarly, Hsu et al. have shown that, using the same imaging equipment as this study and with similar parameters, Ag<sub>2</sub>S NPs produce comparable x-ray contrast to Ag.<sup>10</sup> Here, we explored the x-ray contrast of Ag<sub>2</sub>Te NPs in two main x-ray imaging modalities: CT and DEM. To test the contrast generation of Ag<sub>2</sub>Te NPs in comparison to Ag NPs in both x-ray imaging modalities, experiments using custom-made phantoms were conducted (**Figure 5**).

For CT imaging, the phantom containing the different agents was imaged using a clinical CT system at x-ray energies ranging from 80 kV to 140 kV. **Figure 5A** shows representative images of the different solutions acquired at an x-ray energy of 80 kV. The attenuation rate for Ag<sub>2</sub>Te NPs was higher than that of iopamidol and the other controls, *i.e.* silver nitrate and sodium tellurite, at all studied energies (**Figure 5B**).

For the DEM experiments, the LE and HE energy combinations were explored to find the one yielding the highest contrast for Ag<sub>2</sub>Te (Supplemental Figures 16 - 20). From

this optimization experiment, we selected the energy combination of 29 kV (LE) and 38 kV (HE). **Figure 5C** shows phantom images at LE of 29 kV, HE of 38 kV, and the DE subtraction image. **Figure 5D** shows the quantification of the contrast-to-noise ratio (CNR) of the DE subtraction image for the different solutions. Ag<sub>2</sub>Te NPs exhibit higher CNR than either silver alone or iopamidol, at this LE and HE energy pair (note that we used silver nitrate as a control, which previous experiments have shown to have identical contrast generation to Ag<sub>2</sub>S NPs<sup>10</sup>). Together these phantom studies show that Ag<sub>2</sub>Te NPs exhibit higher contrast than either iopamidol or silver nanoparticles without tellurium and suggest that they could be used as x-ray contrast agents. Of course, this observation is due to the presence of tellurium in Ag<sub>2</sub>Te NPs, but underscores the benefit resulting from ensuring that both elements in the formulation are contrast generating.

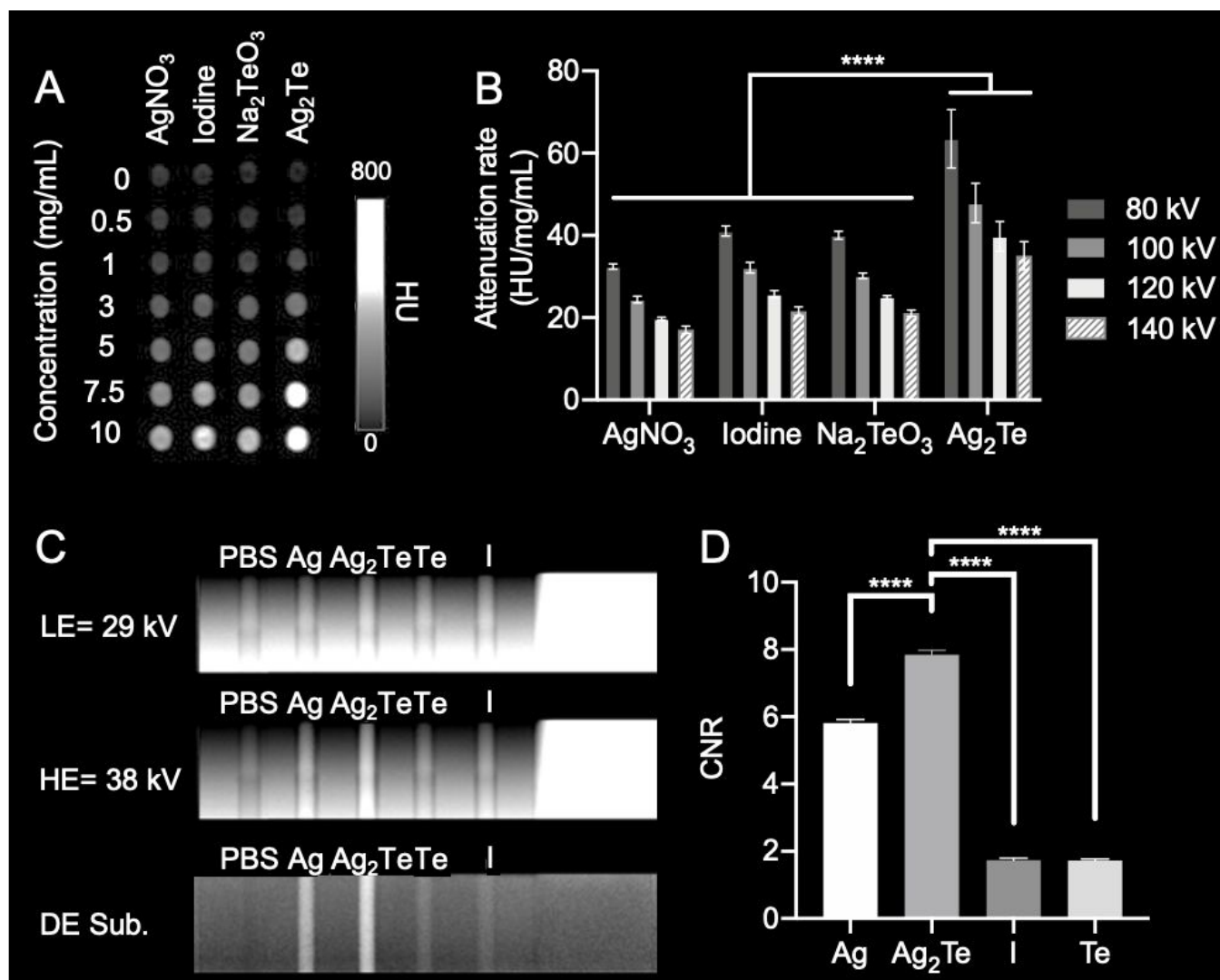


**Figure 5:** *In vitro* imaging with CT and DEM. A) CT phantom image at an energy of 80 kV. B) Quantification of the CT attenuation rate of the different solutions at different energies. Error bars represent standard deviation. C) DEM phantom imaging at a LE of 29 kV, HE of 38 kV, and DEM subtraction image. D) DEM phantom image contrast-to-noise ratio (CNR) quantification. \*\*\*\*  $P \leq 0.0001$ . Ag denotes AgNO<sub>3</sub> salt, Te denotes Na<sub>2</sub>TeO<sub>3</sub> salt, and I denotes iopamidol. PBS was used as a negative control. The

different solutions had a concentration of 10 mg of the element of interest/mL ( $\text{Ag}_2\text{Te}$  NPs had a concentration of 10 mg of Ag/mL to facilitate comparison).

### **$\text{Ag}_2\text{Te}$ NPs lead to high CT contrast in breast cancer tumor-bearing mice**

Our group has previously developed several silver-based DEM and CT contrast agents.<sup>9, 10, 26</sup> Among these, silver sulfide nanoparticles ( $\text{Ag}_2\text{S}$  NPs) have shown promise in their use as DEM and CT contrast agents since they produce contrast, *in vivo*, similar to that of pure silver nanoparticles, but without undesired side effects.<sup>9, 10</sup> To test the *in vivo* contrast of the  $\text{Ag}_2\text{Te}$  NPs, we developed a mouse model by inoculating MDA-MB-231 breast cancer cells to the mice mammary glands. To compare the *in vivo* contrast generation of  $\text{Ag}_2\text{Te}$  NPs with that of  $\text{Ag}_2\text{S}$ , we developed  $\text{Ag}_2\text{S}$  NPs of the same size and coating (5K mPEG-SH) (Supplemental Figure 3 and Supplemental Figure 10), since this should yield similar pharmacokinetics and therefore tumor accumulation for both formulations. Tumor-bearing mice were injected with  $\text{Ag}_2\text{Te}$  NPs or  $\text{Ag}_2\text{S}$  NPs (as a control) at a dose of  $250 \text{ mg Ag}\cdot\text{kg}^{-1}$  (190  $\mu\text{L}$  injection volume). The

tumor-bearing mice were imaged with micro-CT prior to injection and at 2 hrs post- and 24 hrs post-injection. Representative CT images of the heart of tumor-bearing mice at different time points injected with Ag<sub>2</sub>Te NPs are displayed in **Figure 6A**. As presented in **Figure 6B**, an increase in contrast is observed in the heart 2 hrs post-injection. The contrast in the heart can still be observed 24 hrs post-injection. The long circulation time of Ag<sub>2</sub>Te NPs suggests their potential use as blood pool agents for imaging. As expected with nanoparticles of this size, and as shown in Supplemental Figure 21, accumulation was observed in the liver and spleen over 24 hours in both nanoparticle formulations.<sup>26</sup> Moreover, we found the CT attenuation to be higher (compared to pre-injection scans) in the tumors of mice injected with Ag<sub>2</sub>Te NPs than in those of mice injected with Ag<sub>2</sub>S NPs at 2 hrs and 24hrs post-injection (**Figures 6C-D**). No significant difference was found between the NP accumulation in the tumors of mice injected with Ag<sub>2</sub>S and Ag<sub>2</sub>Te (Supplemental Figure 22). This increase in attenuation is as we expected, given the phantom imaging results.

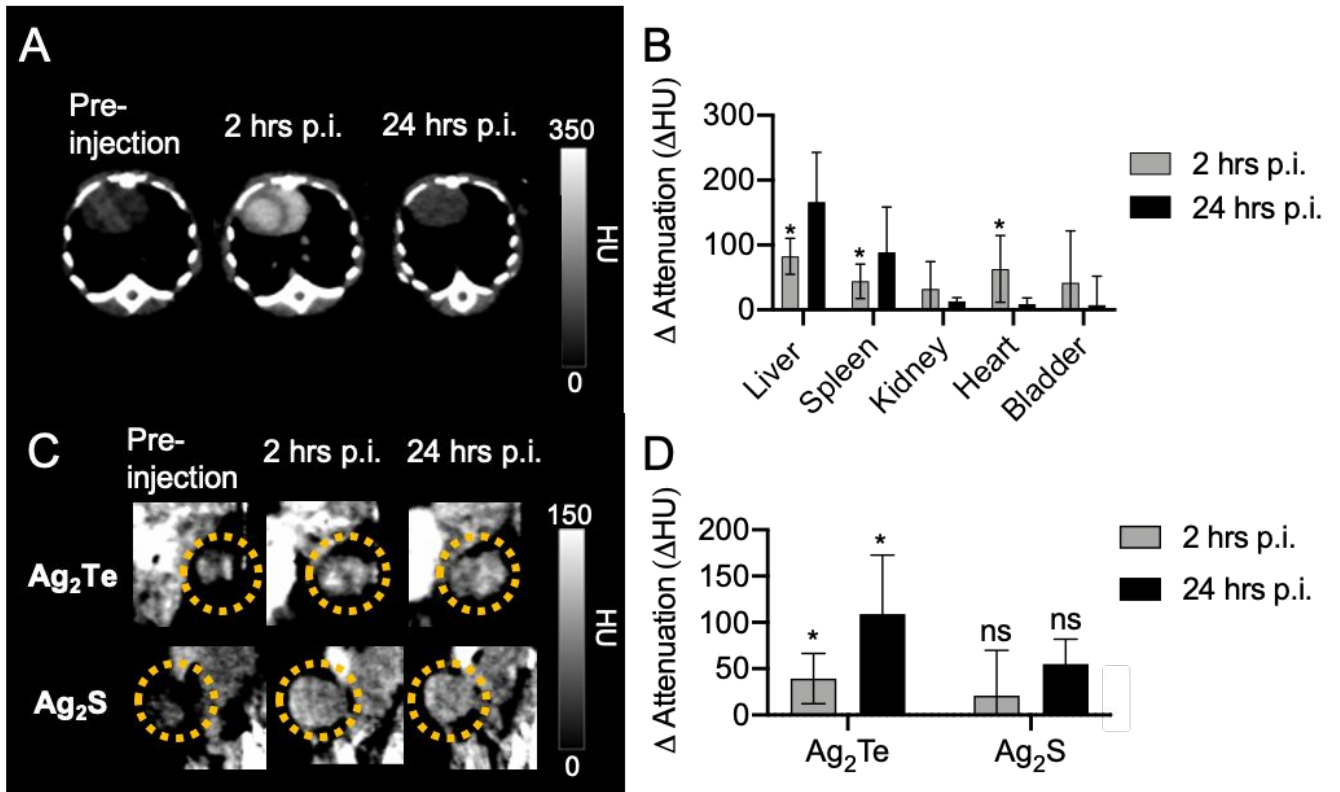


**Figure 6:** *In vivo* CT imaging of breast cancer tumor-bearing mice. A) Representative CT scan images at the level of the heart from a mouse injected with Ag<sub>2</sub>Te NPs, at different time points: pre-injection, 2 hrs post-injection (2 hrs p.i.) and 24 hrs post-injection (24 hrs p.i.). B) Quantification of the change in CT attenuation (difference between pre-injection and the different time point images) in the major organs of mice injected with Ag<sub>2</sub>Te NPs. C) Representative images of CT scans from tumor-bearing mice injected with Ag<sub>2</sub>Te NPs (top row) or Ag<sub>2</sub>S NPs (bottom row). Tumors are highlighted in yellow circles. ROIs matching the outlines of the tumors were used for

image analysis. D) Quantification of the change in CT attenuation in the tumors from mice injected with  $\text{Ag}_2\text{Te}$  or  $\text{Ag}_2\text{S}$  NPs. Error bars represent standard deviation.

Statistical comparisons are versus pre-injection scans. \* $P < 0.05$ .

### **$\text{Ag}_2\text{Te}$ NPs accumulate in RES organs and don't show signs of acute toxicity**

To further investigate the nanoparticle biodistribution, mice were sacrificed 24 hrs post-injection. The organs of both mice groups were collected, and their nanoparticle content was measured through ICP-OES. We found substantial accumulations of  $\text{Ag}_2\text{Te}$  and  $\text{Ag}_2\text{S}$  NPs in the liver and spleen, as expected for nanoparticles of this size<sup>46</sup> (Figure 7A). We observed similar biodistributions for both nanoparticle formulations, which suggests that the observed differences in contrast could be attributed to the incorporation of tellurium to the formulation. In addition, no significant difference was found between the NP accumulation in the tumors of mice injected with  $\text{Ag}_2\text{S}$  and  $\text{Ag}_2\text{Te}$  (Supplemental Figure 23).

To examine the biocompatibility of  $\text{Ag}_2\text{Te}$  NPs *in vivo* we collected sections of tissue of the tumor-bearing mice at 24 hours post-injection and performed hematoxylin and eosin (H&E) staining. Tissues from mice injected with PBS were used as controls (**Figure 7B**). No apparent changes were observed in the tissue structures of  $\text{Ag}_2\text{Te}$  NP-injected mice, with similar morphology found for  $\text{Ag}_2\text{S}$  NPs and PBS-injected mice. These findings support the biocompatibility of the  $\text{Ag}_2\text{Te}$  NPs *in vivo*.

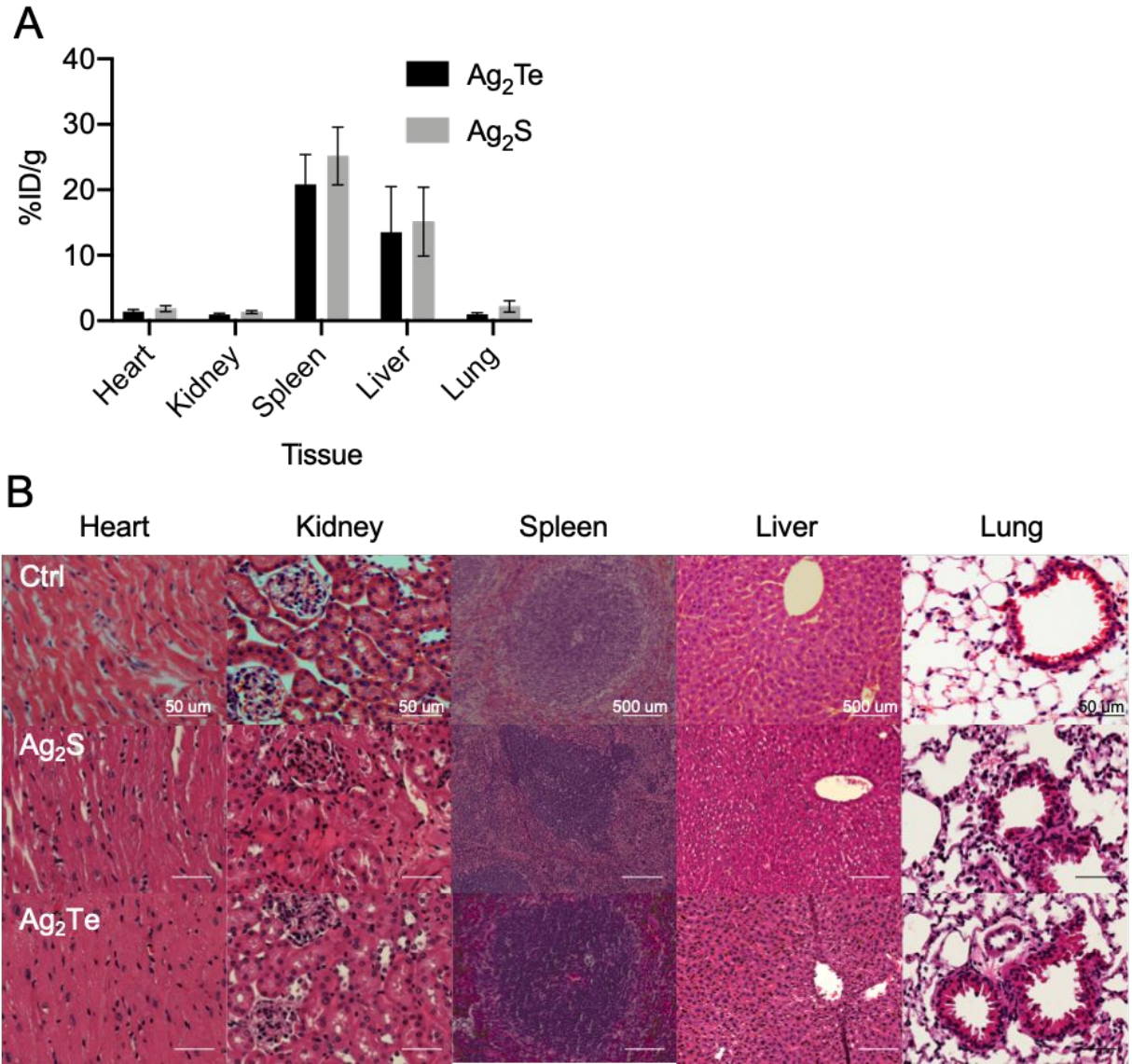


**Figure 7:** A) Biodistribution of Ag<sub>2</sub>Te and Ag<sub>2</sub>S NPs in major tissues and organs of injected mice. Error bars represent standard error of mean (SEM). B) Representative micrographs of tissue from major organs, after H&E staining, of mice injected with saline (top row), Ag<sub>2</sub>S NPs (middle row), and Ag<sub>2</sub>Te NPs (bottom row).

Despite the beneficial optical properties of Ag<sub>2</sub>Te NPs, similar to those reported with other silver chalcogenides, these nanoparticles have not been widely explored for their potential biomedical applications. Up-to-date, only one other group has reported the application of these NPs for biomedical applications *in vivo*.<sup>21</sup> In the study, Zhang *et al.* report the intense fluorescence signal and biocompatibility of Ag<sub>2</sub>Te quantum dots encapsulated in poly(lactic-co-glycolic acid) (PLGA) and coated with cell membrane-derived vesicles. However, this double layer of encapsulation, including the use of a hydrophobic polymer, will limit the possibility for contact of these Ag<sub>2</sub>Te quantum dots with mammalian cells compared with the agents reported in the current study. Moreover, the concentrations used in that study were quite low compared to the concentrations tested in this study. A maximum concentration of particles of 200 µg ml<sup>-1</sup> in the biocompatibility assays and a silver dose of 2 mg kg<sup>-1</sup> for *in vivo* experiments were reported. Although these low concentrations are appropriate for more sensitive applications such as fluorescence imaging, many other biomedical applications require much higher doses, such as radiosensitization or photothermal therapy.<sup>47-52</sup> Herein, we

have explored Ag<sub>2</sub>Te NPs' biomedical application in the setting requiring the highest nanoparticle dose, *i.e.* x-ray imaging.

In this study, we have developed Ag<sub>2</sub>Te NPs of hydrodynamic diameter of  $17 \pm 5$  nm. These nanoparticles not only have excellent biocompatibility with the studied cell lines and *in vivo*, but also generate superior x-ray contrast compared to previously reported silver or silver sulfide nanoparticles.<sup>9, 10, 26, 45</sup> This excellent biocompatibility is likely due in part to their PEGylation, which is known to prevent adverse reactions to exogenous materials, but is also likely due to the extremely low solubility product of Ag<sub>2</sub>Te. This is evidenced from the *in vitro* biocompatibility studies, where we observed reductions in the viability of cells for pure silver nanoparticles, in agreement with prior reports,<sup>43, 51</sup> but not with Ag<sub>2</sub>Te or Ag<sub>2</sub>S NPs. Histology also shows no acute toxicity in the tissue of mice injected with Ag<sub>2</sub>Te. Meanwhile, the high x-ray contrast generating capacity of these NPs, both *in vitro* and *in vivo*, can be largely attributed to the combination of silver and tellurium in the nanoparticles. Our results show higher contrast from Ag<sub>2</sub>Te NPs than would be expected from summing the contributions of the individual elements (**Figure 5D**). This could be due to a phenomenon reported by Kim *et al.* where nanoparticle

contrast agents composed of multiple metals generated higher contrast in CT than the individual elements.<sup>53</sup>

When analyzing the nanoparticle's biodistribution, we observed high accumulation in the liver and spleen 24 hours post-injection. These values are expected due to the nanoparticle's hydrodynamic diameter above the kidney's glomerular filtration threshold (about 5.5 nm).<sup>46</sup> Thus, Ag<sub>2</sub>Te NPs are expected to undergo hepatobiliary elimination,<sup>47</sup> which is an extremely slow process and therefore, Ag<sub>2</sub>Te NPs are expected to remain in the body for an extended period of time.<sup>54, 55</sup> Clinical translation requirements include complete clearance in a reasonable time.<sup>40, 53</sup> To improve clinical translatability, reducing the hydrodynamic diameter of Ag<sub>2</sub>Te NPs to one allowing kidney/urinary clearance, will be desired. Moreover, while our biocompatibility results are encouraging, more extensive studies, such as blood chemistry, repeated dosing, long-term biodistribution, and assessments in larger animal models will be needed to definitively establish safety. In addition, biocompatibility is known to depend on various factors, such as size, shape, and coating, therefore *in vitro* and *in vivo* studies will need to be completed for any new Ag<sub>2</sub>Te NP formulations. Despite the additional work to be done,

our studies provide a good indication of the biomedical applications and translatability of these nanoparticles.

### ***Conclusion***

For the first time, Ag<sub>2</sub>Te NPs have been explored in the *in vivo* setting requiring the highest dose of all biomedical applications: x-ray imaging. Moreover, we have shown the potential utility of these nanoparticles as contrast agents for the screening of breast cancer. Ag<sub>2</sub>Te NPs showed no acute toxicity *in vitro* or *in vivo* as shown by cell viability studies and histological analysis, respectively. Their biocompatibility at this very high dose points to the likelihood that Ag<sub>2</sub>Te NPs will prove to be biocompatible for their many other possible biomedical applications that require lower doses. Furthermore, CT and DEM phantom studies and *in vivo* CT imaging of breast cancer tumor-bearing mice revealed high contrast generation from Ag<sub>2</sub>Te NPs as compared to controls such as a silver salt or Ag<sub>2</sub>S NPs. Moreover, higher contrast was observed in tumors of mice injected with Ag<sub>2</sub>Te NPs when compared to Ag<sub>2</sub>S NPs in CT imaging. Ag<sub>2</sub>Te NPs' good biocompatibility, enhanced contrast, as well their blood pool agent characteristics show

their potential to be used in biomedical applications and, more specifically, as contrast agents for breast cancer screening.

### Supporting information

Supplemental data (PDF file) include synthesis and characterization of Ag NPs and Ag<sub>2</sub>S (TEM micrographs, EDX spectra, UV-visible absorption spectra, and XRD patterns), FT-IR spectra of the different nanoparticles formulations, 11-mercaptopundecanoic acid coated Ag<sub>2</sub>Te as z-potential and stability controls, photograph of DEM phantom, DEM energy pair optimization data, and the quantification of the change in CT attenuation in organs of mice injected with Ag<sub>2</sub>S NPs. This material is available free of charge *via* the Internet at <http://pubs.acs.org>.

### AUTHOR INFORMATION

#### Corresponding Author

\* Corresponding author

E-mail: david.cormode@penntermedicine.upenn.edu; Tel: 215-615-4656; Fax: 215-662-7868

## **Author Contributions**

The project was designed by L.M.N., A.D.A.M, and D.P.C. L.M.N., J.C.H., K.C.L., and D.P.C. performed the experiments. L.M.N and D.P.C. wrote the manuscript. All authors contributed to and have approved the final version of the manuscript.

## **Funding Sources**

This work was supported by funding from NIH (R01-CA227142-02S1 to LMN and R01-CA227142-02 to DPC), NSF (DGE-1845298 to JCH), and the University of Pennsylvania Department of Radiology.

## **Notes**

D.P.C. and A.D.A.M. are named as inventors on patent applications concerning silver-based contrast agents. They also hold stock in Daimroc Imaging, a company that is seeking to commercialize such agents.

## **ACKNOWLEDGMENT**

This work was supported by funding from NIH (R01-CA227142-02S1 to LMN and R01-CA227142-02 to DPC), NSF (DGE-1845298 to JCH), and the University of Pennsylvania Department of Radiology. We thank the Electron Microscopy Resource Laboratory (Sudheer Molugu and Biao Zuo) for their technical support with TEM micrographs and Eric Blankemeyer for his help with micro-CT images. Some illustrations were created with BioRender.com.

## REFERENCES

1. M. Jiao, P. Zhang, J. Meng, Y. Li, C. Liu, X. Luo, M. Gao, *Biomater. Sci.*, 2018, **6**, 726-745.
2. S. Chung, R. A. Revia, M. Zhang, *Adv. Mater.*, 2019, 1904362.
3. Q. Liu, C. Zhan, D. S. Kohane, *Bioconjugate Chem.*, 2017, **28**, 98-104.
4. T. Curry, R. Kopelman, M. Shilo, R. Popovtzer, *Contrast Media Mol. Imaging*, 2014, **9**, 53-61.

5. M. Bouché, J. C. Hsu, Y. C. Dong, J. Kim, K. Taing, D. P. Cormode, *Bioconjugate Chem.*, 2020, **31**, 303-314.
6. X. Han, K. Xu, O. Taratula, K. Farsad, *Nanoscale*, 2019, **11**, 799-819.
7. E. M. Shapiro, *Magn. Reson. Med.*, 2015, **73**, 376-389.
8. L. E. Cole, R. D. Ross, J. M. Tilley, T. Vargo-Gogola, R. K. Roeder, *Nanomedicine (London, U.K.)*, 2015, **10**, 321-341.
9. J. C. Hsu, P. C. Naha, K. C. Lau, P. Chhour, R. Hastings, B. F. Moon, J. M. Stein, W. R. T. Witschey, E. S. McDonald, A. D. A. Maidment, D. P. Cormode, *Nanoscale*, 2018, **10**, 17236-17248.
10. J. C. Hsu, E. D. Cruz, E. K. C. Lau, M. Bouché, J. Kim, A. D. Maidment, D. P. Cormode, *Chem. Mater.*, 2019, **31**, 7845-7854.
11. M. Y. Qin, X. Q. Yang, K. Wang, X. S. Zhang, J. T. Song, M. H. Yao, D. M. Yan, B. Liu, Y. D. Zhao, *Nanoscale*, 2015, **7**, 19484-19492.

12. D. O. Vardar, S. Aydin, I. Hocaoglu, F. H. Y. Acar, N. Basaran, *Chem.-Biol. Interact.*, 2018, **291**, 212-219.
13. H. Tang, S. T. Yang, Y. F. Yang, D. M. Ke, J. H. Liu, X. Chen, H. Wang, Y. Liu, *ACS Appl. Mater. Interfaces*, 2016, **8**, 17859-17869.
14. Y. P. Gu, R. Cui, Z. L. Zhang, Z. X. Xie, D. W. Pang, *J. Am. Chem. Soc.*, 2012, **134**, 79-82.
15. E. A. Buketov, M. Z. Ugorets, A. S. Pashinkin, *Russ. J. Inorg. Chem.*, 1964, **9**, 292-294.
16. M. Yang, R. Gui, H. Jin, Z. Wang, F. Zhang, J. Xia, S. Bi, Y. Xia, *Colloids Surf., B*, 2015, **126**, 115-120.
17. C. Lu, G. Chen, B. Yu, H. Cong, *Advanced Engineering Materials*, 2018, **20**, 1700940.
18. R. Karunamuni, A. D. Maidment, *Phys. Med. Biol.*, 2014, **59**, 4311-4324.
19. H. Jin, R. Gui, J. Sun, Y. Wang, *Colloids Surf. B*, 2016, **143**, 118-123.

20. C. W. Wang, Z. H. Lin, P. Roy, H. T. Chang, *Front. Chem.*, 2013, **1**, 1-5.
21. J. J. Zhang, Y. Lin, H. Zhou, H. He, J. J. Ma, M. Y. Luo, Z. L. Zhang, D. W. Pang, *Adv. Healthc. Mater.*, 2019, **8**, 1900341.
22. H. Lusic, M. W. Grinstaff, *Chem. Rev.*, 2013, **113**, 1641-1666.
23. T. A. Rose, J. W. Choi, *Am. J. Med.*, 2015, **128**, 943-949.
24. M. A. Shahbazi, L. Faghfour, M. P. A. Ferreira, P. Figueiredo, H. Maleki, F. Sefat, J. Hirvonen and H. A. Santos, *Chem Soc Rev*, 2020, **49**, 1253-1321.
25. H. Chen, H. Paholak, M. Ito, K. Sansanaphongpricha, W. Qian, Y. Che, D. Sun, *Nanotechnology*, 2013, **24**, 355101.
26. P. C. Naha, K. C. Lau, J. C. Hsu, M. Hajfathalian, S. Mian, P. Chhour, L. Uppuluri, E. S. McDonald, A. D. Maidment, D. P. Cormode, *Nanoscale*, 2016, **8**, 13740-13754.
27. K. C. Lau, J. C. Hsu, P. C. Naha, P. Chhour, R. Hastings, J. M. Stein, E. S. McDonald, D. P. Cormode, A. D. Maidment, *Proc. SPIE*, 2018, **10718**, 107180N.

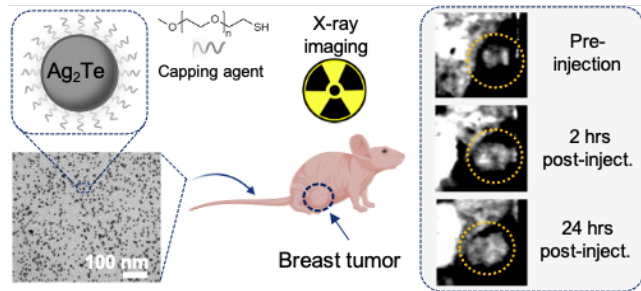
28. M. S. Jochelson, D. D. Dershaw, J. S. Sung, A. S. Heerdt, C. Thornton, C. S. Moskowitz, J. Ferrara, E. A. Morris, *Radiology*, 2013, **266**, 743-751.
29. A. Silvestri, D. Di Silvio, I. Llarena, R. A. Murray, M. Marelli, L. Lay, L. Polito, S. E. Moya, *Nanoscale*, 2017, **9**, 14730-14739.
30. W. Wang, Q. Q. Wei, J. Wang, B. C. Wang, S. H. Zhang, Z. Yuan, *J. Colloid Interface Sci.*, 2013, **404**, 223-229.
31. K. Rahme, L. Chen, R. G. Hobbs, M. A. Morris, C. O'Driscoll, J. D. Holmes, *Rsc Advances*, 2013, **3**, 6085-6094.
32. J. D. Clogston, A. K. Patri, Zeta Potential Measurement. In Characterization of Nanoparticles Intended for Drug Delivery, McNeil, S. E., Ed. Humana Press: Totowa, NJ, 2011, 63-70.
33. Q. Xiao, Y. Liang, Y. Liu, S. Lu, S. Huang, *Luminescence*, 2018, **33**, 181-189.
34. R. Gui, H. Jin, Z. Wang, L. Tan, *Coordination Chemistry Reviews*, 2015, **296**, 91-124.

35. Y. Shen, J. Lifante, E. Ximendes, H. D. Santos, D. Ruiz, B. H. Juárez, I. Z. Gutiérrez, V. T. Vera, J. R. Retama, E. M. Rodríguez, *Nanoscale*, 2019, **11**, 19251-19264.
36. L. J. Shi, C. N. Zhu, H. He, D. L. Zhu, Z. L. Zhang, D. W. Pang, Z. Q. Tian, *RSC advances* 2016, **6**, 38183-38186.
37. D. Cadavid, M. Ibáñez, A. Shavel, O. J. Durá, M. L. de la Torre, A. Cabot, *J. Mater. Chem. A*, 2013, **1**, 4864-4870.
38. S. Gholamrezaei, M. Salavati-Niasari, D. Ghanbari, S. Bagheri, *Sci. Rep.*, 2016, **6**, 20060.
39. A. Mukhopadhyay, N. Joshi, K. Chattopadhyay, G. De, *ACS Appl. Mater. Interfaces*, 2012, **4**, 142-149.
40. M. B. Ahmad, M. Y. Tay, K. Shameli, M. Z. Hussein, J. J. Lim, *Int. J. Mol. Sci.*, 2011, **12**, 4872-4884.

41. N. Hoshyar, S. Gray, H. Han, G. Bao, *Nanomedicine (London, U.K.)*, 2016, **11**, 673-692.
42. M. Yu, J. Zheng, *ACS Nano*, 2015, **9**, 6655-6674.
43. Q. Feng, Y. Liu, J. Huang, K. Chen, K. Xiao, *Sci. Rep.*, 2018, **8**, 2082.
44. N. Durán, C. P. Silveira, M. Durán, D. S. Martinez, *J. Nanobiotechnol.*, 2015, **13**, 55.
45. R. Karunamuni, A. Tsourkas, A. D. Maidment, *Br. J. Radiol.*, 2014, **87**, 20140081.
46. Y. C. Dong, M. Hajfathalian, P. S. N. Maidment, J. C. Hsu, P. C. Naha, S. Si-Mohamed, M. Breuilly, J. Kim, P. Chhour, P. Douek, H. I. Litt, D. P. Cormode, *Sci. Rep.*, 2019, **9**, 14912.
47. C. Li, X. Q. Yang, M. Z. Zhang, Y. Y. Song, K. Cheng, J. An, X. S. Zhang, Y. Xuan, B. Liu, Y. D. Zhao, *Theranostics*, 2018, **8**, 5662-5675.
48. Y. Xu, X. Wang, L. Cheng, Z. Liu, Q. Zhang, *Chem. Eng. J.*, 2019, **378**, 122025.

49. K. Yang, L. Hu, X. Ma, S. Ye, L. Cheng, X. Shi, C. Li, Y. Li, Z. Liu, *Adv. Mater.*, 2012, **24**, 1868-1872.
50. T. Paunesku, S. Gutiontov, K. Brown, G. E. Woloschak, *Cancer Treat. Res.*, 2015, **166**, 151-171.
51. M. Laprise-Pelletier, T. Simão, M. A. Fortin, *Adv. Healthc. Mater.*, 2018, **7**, 1701460.
52. B. Zhu, Y. Li, Z. Lin, M. Zhao, T. Xu, C. Wang, N. Deng, *Nanoscale Res. Lett.*, 2016, **11**, 198.
53. J. Kim, A. B. Silva, J. C. Hsu, P. S. Maidment, N. Shapira, P. B. Noël, D. P. Cormode, *Chem. Mater.*, 2020, **32**, 381-391.
54. Y. N. Zhang, W. Poon, A. J. Tavares, I. D. McGilvray, W. C. W. Chan, *J. Control Release*, 2016, **240**, 332-348.
55. H. S. Choi, W. Liu, P. Misra, E. Tanaka, J. P. Zimmer, B. I. Ipe, M. G. Bawendi, J. V. Frangioni, *Nat. Biotechnol.*, 2007, **25**, 1165-1170.



*Table of contents graphic*

Silver telluride nanoparticle's ( $\text{Ag}_2\text{Te}$  NPs) show good biocompatibility, enhanced contrast, and blood pool agent characteristics and thus could be used contrast agents for breast cancer screening.